






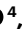








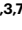

Imaging moiré excited states with photocurrent tunnelling microscopy

Received: 5 April 2023

Accepted: 6 November 2023

Published online: 3 January 2024

 Check for updates


Hongyuan Li ^{1,2,3,10}, Ziyu Xiang^{1,2,3,10}, Mit H. Naik ^{1,3,10}, Wochang Kim ^{1,3}, Zhenglu Li ^{1,3}, Renee Sailus ⁴, Rounak Banerjee ⁴, Takashi Taniguchi ⁵, Kenji Watanabe ⁶, Sefaattin Tongay ⁴, Alex Zettl ^{1,3,7}, Felipe H. da Jornada ^{8,9}, Steven G. Louie ^{1,3} , Michael F. Crommie ^{1,3,7}  & Feng Wang ^{1,3,7} 

Moiré superlattices provide a highly tuneable and versatile platform to explore novel quantum phases and exotic excited states ranging from correlated insulators to moiré excitons. Scanning tunnelling microscopy has played a key role in probing microscopic behaviours of the moiré correlated ground states at the atomic scale. However, imaging of quantum excited states in moiré heterostructures remains an outstanding challenge. Here we develop a photocurrent tunnelling microscopy technique that combines laser excitation and scanning tunnelling spectroscopy to directly visualize the electron and hole distribution within the photoexcited moiré exciton in twisted bilayer WS_2 . The tunnelling photocurrent alternates between positive and negative polarities at different locations within a single moiré unit cell. This alternating photocurrent originates from the in-plane charge transfer moiré exciton in twisted bilayer WS_2 , predicted by our *GW*-Bethe–Salpeter equation calculations, that emerges from the competition between the electron–hole Coulomb interaction and the moiré potential landscape. Our technique enables the exploration of photoexcited non-equilibrium moiré phenomena at the atomic scale.

Two-dimensional (2D) moiré superlattices exhibit novel correlated ground and excited states ranging from correlated insulators^{1–17} and superconductivity^{18–20} to moiré excitons^{7–10,21}. Although measurements such as electrical transport^{16,20,22,23} and optical spectroscopy^{2–4} have revealed mesoscopic properties of the moiré correlated phenomena, knowledge about their microscopic nature is still limited. Such microscopic study is particularly important to understand how these correlated phenomena are affected by the interplay between charge,

orbitals and lattices. Scanning tunnelling microscopy (STM) has played an indispensable role in exploring the moiré physics at the nanometre scale^{1,11–15,24}, which provides real-space information on various correlated ground states such as Mott insulators^{11–15}, electron crystals^{1,17} and superconductivity^{18,19}. However, so far little progress has been made on exploring the moiré excited states at the nanometre scale. Probing individual electrons and holes in the transient excited states is intrinsically challenging since it requires high spatial resolution,

¹Department of Physics, University of California at Berkeley, Berkeley, CA, USA. ²Graduate Group in Applied Science and Technology, University of California Berkeley, Berkeley, CA, USA. ³Materials Sciences Division, Lawrence Berkeley National Laboratory, Berkeley, CA, USA. ⁴School for Engineering of Matter, Transport and Energy, Arizona State University, Tempe, AZ, USA. ⁵International Center for Materials Nanoarchitectonics, National Institute for Materials Science, Tsukuba, Japan. ⁶Research Center for Functional Materials, National Institute for Materials Science, Tsukuba, Japan. ⁷Kavli Energy Nano Sciences Institute, University of California Berkeley and Lawrence Berkeley National Laboratory, Berkeley, CA, USA. ⁸Department of Materials Science and Engineering, Stanford University, Palo Alto, CA, USA. ⁹Stanford Institute for Materials and Energy Sciences, SLAC National Accelerator Laboratory, Menlo Park, CA, USA. ¹⁰These authors contributed equally: Hongyuan Li, Ziyu Xiang, Mit H. Naik.

 e-mail: sglouie@berkeley.edu; crommie@physics.berkeley.edu; fengwang76@berkeley.edu

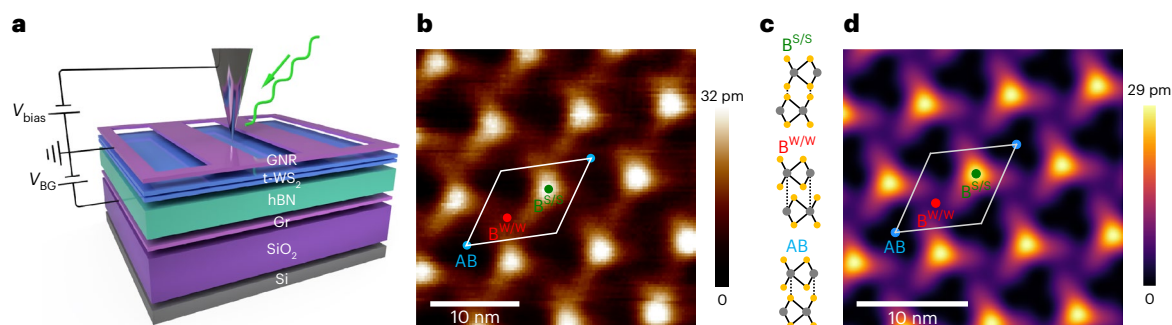


Fig. 1 | Laser-STM measurements of a twisted bilayer WS₂ moiré superlattice. **a**, A sketch of the experimental set-up for laser-STM measurements of a near-58° t-WS₂ bilayer device. The t-WS₂ is placed on top of 49-nm-thick hBN and a graphite (Gr) substrate (that serve as the gate dielectric and back gate). A back gate voltage V_{BG} is applied between the t-WS₂ and the graphite back gate. A graphene nanoribbon array (GNR) is placed on top of the t-WS₂ to serve as the contact electrode. A sample–tip bias V_{bias} is applied between the t-WS₂ and the STM tip

to induce a tunnel current. A 520-nm-wavelength continuous wave laser (wavy green line) is focused on the tip tunnel junction. **b**, A typical STM topography image of the t-WS₂ surface, exhibiting the triangular moiré lattice. $V_{bias} = -4$ V, $I = 100$ pA. Three high-symmetry stacking regions (B^{S/S}, B^{W/W} and AB) are labelled with solid dots. **c**, An illustration of the B^{S/S}, B^{W/W} and AB stacking structures. Yellow and grey dots represent S and W atoms, respectively. **d**, The theoretically calculated surface height variation for t-WS₂.

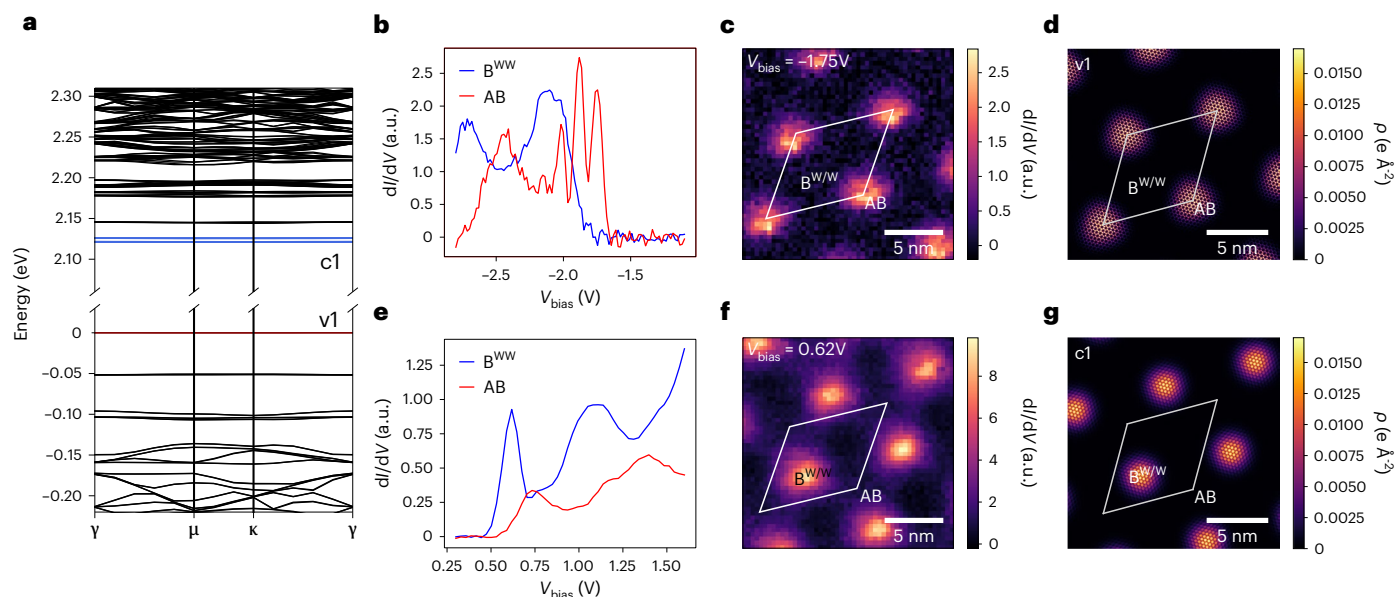


Fig. 2 | Electronic structure of twisted bilayer WS₂. **a**, The calculated electronic band structure of the t-WS₂ moiré superlattice. The moiré flat bands at the valence band top and conduction band bottom are labelled ‘v1’ and ‘c1’. **b**, The dI/dV spectra measured at the B^{W/W} (blue) and AB (red) stacking sites for the valence band. The AB site shows a first sharp peak near $V_{bias} = -1.75$ V. **c, d**, The t-WS₂ dI/dV map measured at $V_{bias} = -1.75$ V (**c**) and the calculated charge density

(ρ) distribution for v1 (**d**), both showing strong hole localization at the AB site. $V_{BG} = -2$ V for **b** and **c, e**. The dI/dV spectra measured at the B^{W/W} (blue) and AB (red) stacking sites for the conduction band. The B^{W/W} site shows a first sharp peak near $V_{bias} = 0.60$ V. **f, g**, The t-WS₂ dI/dV map measured at $V_{bias} = 0.62$ V (**f**) and the calculated charge density (ρ) distribution for c1 (**g**), both showing strong electron localization at the B^{W/W} site. $V_{BG} = 1.5$ V for **e** and **f**.

charge sensitivity and effective excitation, which is beyond the capability of typical optical spectroscopy techniques. There has been recent effort on using photoemission spectroscopy¹¹ and electron excitation¹² to microscopically probe the moiré excited states, which, however, still cannot spatially resolve the internal structures of the photoexcited holes and electrons. In this Article, we describe the combination of laser excitation with STM (termed laser-STM) to probe the individual electron and hole properties in moiré excited states at the nanoscale. We developed a photocurrent tunnelling microscopy (PTM) technique based on laser-STM, which enabled us to measure the internal microscopic structure of photoexcited states in near-60° twisted WS₂ (t-WS₂) bilayers and reveal the emergence of the in-plane charge transfer (ICT) moiré excitons. Related laser-STM methods have been used to probe photoexcitation in molecule systems^{25–28} and conventional bulk semiconductors^{29–34}.

Results

Figure 1a shows an illustration of our gate-tuneable t-WS₂ device and laser-STM set-up (see also Supplementary Fig. 1). The t-WS₂ sits on top of a 49-nm-thick layer of hexagonal boron nitride (hBN) which is placed above a graphite back gate. A back gate voltage (V_{BG}) is applied between the t-WS₂ and the graphite back gate to control the carrier density in the t-WS₂. We use a graphene nanoribbon array electrode on the t-WS₂ surface to make the sample conductive enough for STM measurements³⁵. A bias voltage (V_{bias}) is applied to the t-WS₂ relative to the STM tip to induce a tunnel current. Details of the device fabrication are included in Methods section.

Figure 1b shows a typical STM topography image of the t-WS₂ surface and features a moiré superlattice with a moiré period of approximately 9 nm. Three high-symmetry stacking regions can be seen within the moiré unit cell: the dark (bright) areas correspond to AB (B^{S/S})

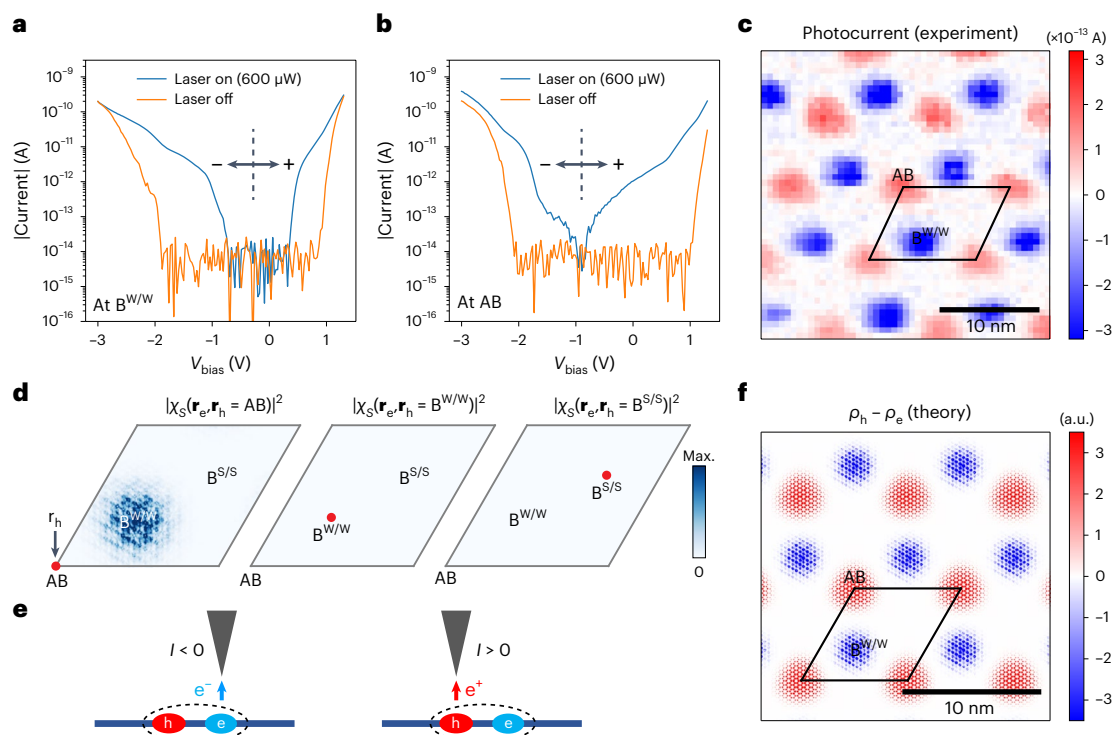


Fig. 3 | Photocurrent mapping of ICT excitons. **a, b.** The STM tunnel current spectra measured at the $B^{W/W}$ (**a**) and AB stacking sites (**b**) with the laser turned off (orange) and on (blue). $V_{BG} = 0$. The absolute value of the current is plotted on a logarithmic scale (where the left and right branch of the spectra correspond to negative and positive current, respectively). For the laser-off case, the current at both the $B^{W/W}$ and the AB sites indicate an energy gap for $-2 \text{ V} < V_{\text{bias}} < 1 \text{ V}$. For the laser-on case ($P = 600 \mu\text{W}$), photocurrent emerges in the energy gap region and the $B^{W/W}$ and AB sites show different photocurrent spectral shapes. **c.** A photocurrent map of t- WS_2 measured with the laser on ($P = 600 \mu\text{W}$) for $V_{\text{bias}} = -0.60 \text{ V}$ and $V_{\text{BG}} = 0$, showing positive (negative) photocurrent at the AB

($B^{W/W}$) sites. **d.** The calculated electron density for the lowest energy exciton, $|\chi_0(\mathbf{r}_e, \mathbf{r}_h)|^2$, with fixed hole position \mathbf{r}_h (solid red dot) at the AB site (left), the $B^{W/W}$ site (middle) and the $B^{S/S}$ site (right). The maps show appreciable electron density at the $B^{W/W}$ site only when the hole position is fixed at the AB site (left). Max., maximum. **e.** A schematic showing the tip-position-dependent tunnel current from an ICT exciton. When the STM tip sits above the electron (left), the larger tunnel probability for the electron yields a negative current. A positive current is detected when the tip sits above the hole (right). **f.** The calculated charge distribution map $\rho(\mathbf{r}) = \rho_h(\mathbf{r}) - \rho_e(\mathbf{r})$ of the ICT exciton, where $\rho_h(\mathbf{r}) = \int |\chi_0(\mathbf{r}_e, \mathbf{r}_h)|^2 d\mathbf{r}_e$ and $\rho_e(\mathbf{r}) = \int |\chi_0(\mathbf{r}_e, \mathbf{r}_h)|^2 d\mathbf{r}_h$.

stacking regions, while the intermediate height area is a $B^{W/W}$ stacking region. Model structures for the AB, $B^{S/S}$ and $B^{W/W}$ stacking regions are illustrated in Fig. 1c. This topography agrees well with our calculated height distribution map (Fig. 1d) and arises owing to an out-of-plane reconstruction that leads to strong variation in the local interlayer spacing (see Supplementary Information for details). The $B^{S/S}$ stacking regions have the largest interlayer spacing owing to steric hindrance arising from the S atoms of the top and bottom layers facing each other³⁶. In-plane reconstruction of the superlattice leads to a noticeably larger area for the low-energy AB stacking region and results in strain redistribution in the two WS_2 layers (see Supplementary Information for details). The final relaxed structure reflects a trade-off between the energy gain from forming large-area AB stacking regions and the energy cost of strain redistribution.

We characterized the single-particle electronic structure of t- WS_2 by applying scanning tunnelling spectroscopy and comparing the results with theoretical calculations. Figure 2a shows the calculated electronic band structure of a t- WS_2 moiré superlattice with a period of 9 nm, including spin-orbit coupling. Here, we are mainly concerned with the moiré flat bands at the valence band top (labelled 'v1') and the conduction band bottom (labelled 'c1'), which host the lowest energy holes and electrons, respectively. The computed flat bands arise from a deep triangular quantum well potential due to the inhomogeneous layer hybridization and structural reconstruction^{36,37} which yield narrow bandwidths of 1 meV and 5 meV for the v1 and c1 bands, respectively. The v1 band is derived from states near the Γ point in the pristine unit cell Brillouin zone (BZ) and is twofold degenerate,

while the c1 states are folded from around the Q point of the pristine unit cell BZ and comprise two closely spaced bands (each with sixfold degeneracy). The small splitting in energy of these two sets of c1 bands is induced by interlayer hybridization. The spatial distribution of these moiré flat bands is experimentally reflected by the differential conductance (dI/dV) spectra measured at the $B^{W/W}$ and AB sites (Fig. 2b,e). On the valence band side (Fig. 2b), the AB site shows a sharp peak at around $V_{\text{bias}} = -1.75 \text{ V}$ while the $B^{W/W}$ site exhibits almost no signal until $V_{\text{bias}} = -1.85 \text{ V}$, indicating that the twofold-degenerate v1 band is mainly localized on the AB site. This spatial distribution was confirmed by dI/dV mapping measured at $V_{\text{bias}} = -1.75 \text{ V}$ (Fig. 2c), which matches the calculated v1 band's charge density (ρ) distribution (Fig. 2d), both of which show maximum density at the AB site. On the conduction band side (Fig. 2e), the lowest energy dI/dV peak appears at the $B^{W/W}$ site at $V_{\text{bias}} = 0.60 \text{ V}$ while the AB site exhibits a small signal until $V_{\text{bias}} = 0.75 \text{ V}$, indicating that the c1 band states are mainly localized on the $B^{W/W}$ site. This was also confirmed by dI/dV mapping measured at $V_{\text{bias}} = 0.62 \text{ V}$ (Fig. 2f), which matches the calculated c1 bands' charge density distribution (Fig. 2g), both of which show maximum density at the $B^{W/W}$ site. These results show that a strong moiré potential exists in t- WS_2 and that the lowest energy single-particle electron and hole states are spatially separated (see Supplementary Information for more details on the calculations). We note that a moiré superlattice modifies photoexcited states in different ways depending on the strength and shape of the moiré potential. Weak moiré potentials, for example, generate Umklapp scattering of the pristine Wannier excitons that leads to some spatial modulation while retaining their overall Wannier

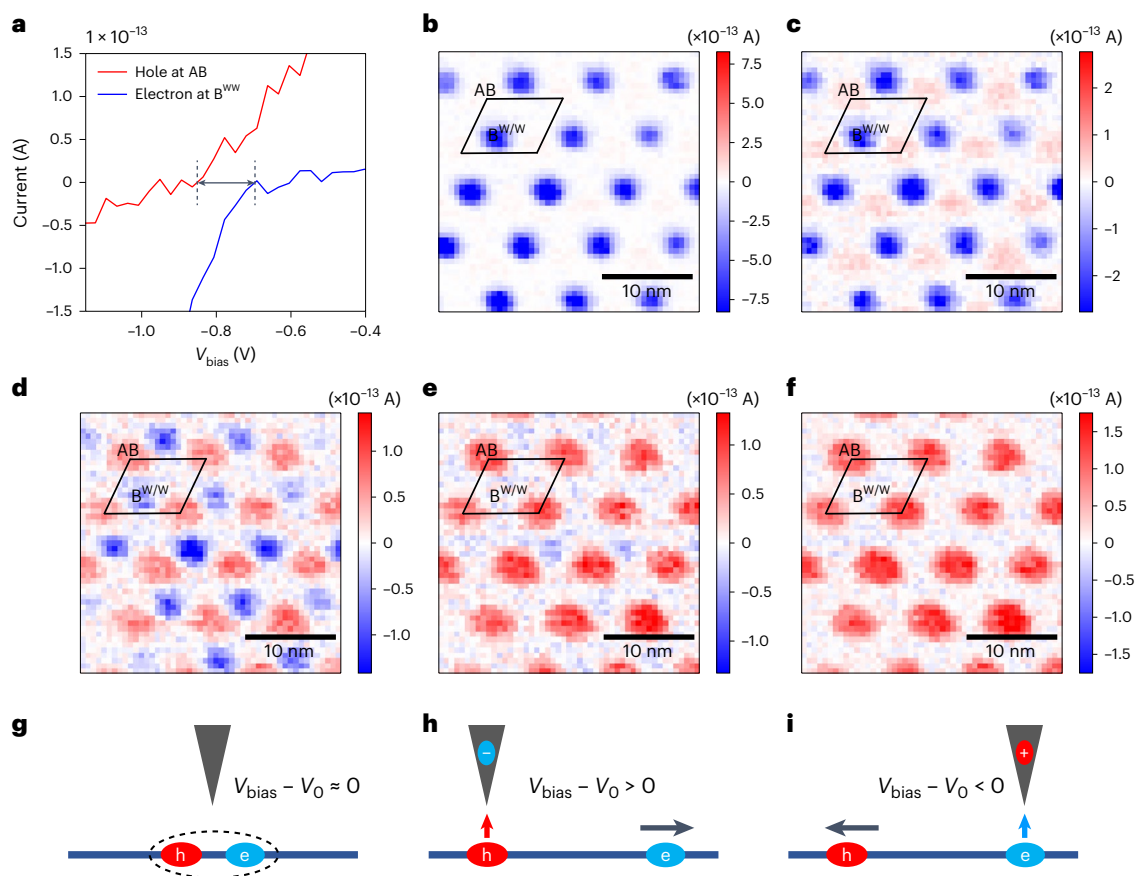


Fig. 4 | Interaction between STM tip and ICT excitons. **a**, A zoom-in of the photocurrent spectra at the AB (hole) site (red) and the B^{W/W} (electron) site (blue). Spatially alternating current polarity occurs for a V_{bias} range of approximately 200 mV (arrow and dashed lines). **b–f**, The evolution of the t-WS₂ photocurrent map for increasing V_{bias} values of -985 mV (**b**), -889 mV (**c**), -793 mV (**d**), -697 mV (**e**) and -602 mV (**f**). Spatially alternating current polarity exists only in **c–e**, while negative (positive) current dominates in **b** (**f**). **g–i**, The tip-induced ICT exciton

dissociation effect. V_0 is the bias voltage offset that compensates the work function difference between the tip and the back gate graphite: for $V_{\text{bias}} - V_0 \approx 0$, the tip does not strongly perturb the ICT exciton and so both photocurrent polarities are seen (**g**); for $V_{\text{bias}} - V_0 > 0$, negative charge accumulates at the tip apex, which attracts holes and repels electrons, thereby dissociating ICT excitons (**h**); for $V_{\text{bias}} - V_0 < 0$, the tip attracts electrons and repels holes, thereby dissociating ICT excitons (**i**).

characteristics³⁸. Strong moiré potentials, such as those created by strain-induced reconstructions in transition metal dichalcogenides (TMD) bilayers, not only induce Umklapp scattering of excitons but can also alter the internal structure of moiré excitons¹⁰.

To experimentally probe the excitonic states, we illuminated our t-WS₂ device with a 520 nm continuous wave laser focused on the tip-sample tunnel junction (Supplementary Fig. 1). Real-time feedback control of the laser alignment was performed to maintain a stable laser spot relative to the tip position (Methods). Photoexcited electrons and holes in t-WS₂ relax quickly (on the time scale of picoseconds) to the lowest energy moiré exciton state through phonon emission^{39–41}. Here, we set the back gate voltage V_{BG} to near 0 to keep the t-WS₂ undoped, so as to avoid free carrier scattering that could decrease the exciton lifetime⁴² (see Supplementary Section S8 for more details on the impact of non-zero V_{BG}). The spatial charge distribution of the lowest energy (long lived) moiré exciton state was probed through STM tunnelling photocurrent measurements (as electron tunnelling processes occur on the time scale of nanoseconds). Figure 3a,b show the absolute value of the tunnel current (I) as a function of V_{bias} measured at B^{W/W} and AB stacking sites with (blue) and without (orange) laser illumination (measured with a laser power of $P = 600 \mu\text{W}$ and a laser illumination area of around $80 \mu\text{m}^2$; see Supplementary Section S9 for the power dependence). When the laser is off, the tunnel current for both stacking sites shows a large semiconducting bandgap for $-2 \text{ V} < V_{\text{bias}} < 1 \text{ V}$. However, when the laser is turned on, a photocurrent emerges even when V_{bias}

lies in this gap region and the photocurrent response at the B^{W/W} and AB sites show very different behaviour. There is a V_{bias} region where the positive photocurrent at the B^{W/W} site (Fig. 3a) and the negative photocurrent at the AB site (Fig. 3b) can be observed simultaneously. We denote the centre of this V_{bias} region as V_0 . As explained below, V_0 changes between -800 mV and -300 mV depending on the STM tip status, for example, owing to changes of the atomic structure at the tip (after tip fixing and reshaping) or an adsorbed molecule on the tip, which can modify the tip work function and shift V_0 . The data in Figs. 3a,b and 4 were obtained using an STM tip with $V_0 = -790$ mV.

To investigate the spatial dependence of the tunnelling photocurrent, we performed 2D photocurrent mapping with $V_{\text{bias}} = -0.60$ V and $V_{\text{BG}} = 0$ (Fig. 3c). The laser power was held at $P = 600 \mu\text{W}$. The STM tip configuration has $V_0 = -0.60$ V in this set of measurements. Surprisingly, the photocurrent changes sign at different locations even for fixed V_{bias} . Positive photocurrent (red) appears at AB sites, while negative photocurrent (blue) appears at B^{W/W} sites. This spatially alternating photocurrent polarity provides direct experimental evidence for the emergence of ICT moiré excitons.

To better interpret the photocurrent spatial distribution, we performed calculations of the excitonic states of t-WS₂ using ab initio *GW*-BSE (refs. 43,44) calculations. Here, the exciton wavefunction χ_S is expressed as a linear combination of single-particle conduction ($c_{\mathbf{k}_m}$) and valence states ($v_{\mathbf{k}_m}$) in the moiré BZ: $\chi_S(\mathbf{r}_e, \mathbf{r}_h) = \sum_{c\nu\mathbf{k}_m} A_{c\nu\mathbf{k}_m}^S \Psi_{\nu\mathbf{k}_m}^*(\mathbf{r}_h) \Psi_{c\mathbf{k}_m}(\mathbf{r}_e)$, where S is the exciton principal quantum number, \mathbf{k}_m is the electron

wave vector in the moiré BZ, \mathbf{r}_e and \mathbf{r}_h are the electron and hole coordinates, respectively, ν and c label a valence and conduction band, respectively, and $A_{\nu c k_m}^S$ are exciton electron–hole expansion coefficients. The exciton states can be calculated (including electron and hole degree of freedom) by state-of-the-art full-spinor *GW*-BSE calculations. However, owing to the large number of atoms ($\sim 4,000$) in the t-WS₂ moiré unit cell, this calculation is computationally intractable.

To overcome this bottleneck, we developed a new computational algorithm for calculating the electron–hole interaction kernel matrix elements. This involves extending the pristine unit cell matrix projection (PUMP) method (developed previously for reconstructed monolayers⁸) to bilayer moiré superlattices. In the new scheme, the wavefunction of each valence ($|\psi_{\nu k_m}\rangle$) and conduction ($|\psi_{c k_m}\rangle$) state in the moiré BZ is expressed as a linear combination of many states of the pristine individual layers: $|\psi_{\nu k_m}\rangle = \sum_i a_i^{\nu k_m} |\phi_{a, i k_m}^{\text{val}}\rangle + b_i^{\nu k_m} |\phi_{b, i k_m}^{\text{val}}\rangle$ and $|\psi_{c k_m}\rangle = \sum_i a_i^{c k_m} |\phi_{a, i k_m}^{\text{cond}}\rangle + b_i^{c k_m} |\phi_{b, i k_m}^{\text{cond}}\rangle$, where ϕ_a and ϕ_b refer to the pristine superlattice wavefunctions of the bottom and top WS₂ layer, respectively. The pristine superlattice states are related to states in the rotated pristine BZs of the individual layers by band folding. Using the set of expansion coefficients $a_i^{\nu k_m}$, $a_i^{c k_m}$ and $b_i^{c k_m}$, we approximate each moiré electron–hole interaction kernel matrix element in the BSE as a coherent sum over many pristine unit cell kernel matrix elements. This generalized PUMP method allows us to calculate moiré exciton energies and wavefunctions for the t-WS₂ moiré superlattice (see Supplementary Information for more details). We study the $\mathbf{Q} = 0$ exciton in the moiré BZ, where \mathbf{Q} is the exciton centre-of-mass wave vector. While these states are formed by coherent superposition of direct transitions in the moiré BZ, the valence band and conduction band states involved originate from different valleys in the unfolded unit cell BZ and are strongly modified by the moiré potential.

Figure 3d shows the calculated electron density distribution for the lowest energy exciton wavefunction $\chi_0(\mathbf{r}_e, \mathbf{r}_h)$ with a fixed hole position \mathbf{r}_h (labelled with a solid red dot) at the AB site (left panel), the B^{W/W} site (middle panel) and the B^{S/S} site (right panel). The electron density is maximum at the B^{W/W} site when the hole is at the AB site and is vanishingly small when the hole is at the B^{W/W} and B^{S/S} sites. The spin-aligned and spin-anti-aligned excitons have the same energy owing to the spatial separation of the photoexcited electron and hole, which results in a small exchange energy. In the out-of-plane direction, the electron and hole charge densities are delocalized over both layers and show no interlayer charge transfer. This demonstrates that the lowest energy exciton state in t-WS₂ is a layer-hybridized ICT exciton, in which the electron and hole prefer the B^{W/W} site and AB site, respectively. The calculated binding energy for the ICT exciton, when the bilayer is suspended in vacuum, is ~ 150 meV. In the presence of the hBN substrate, we expect the binding energy to be smaller owing to additional dielectric screening.

ICT moiré excitons can be expected to yield a STM tip position-dependent photocurrent polarity owing to their intrinsic lateral electron–hole separation. As illustrated in Fig. 3e, when the STM tip is parked above the photoexcited electron of an ICT exciton (left panel), the tunnelling probability for the electron dominates compared with the spatially displaced photoexcited hole, thus resulting in negative tunnelling current. Similarly, positive tunnel current is expected when the tip is parked above the photoexcited hole (right panel). Our photocurrent measurements thus directly reflect the charge density distribution of the lowest energy ICT moiré exciton, which can be expressed in units of proton charge as $\rho(\mathbf{r}) = \rho_h(\mathbf{r}) - \rho_e(\mathbf{r})$, where $\rho_e(\mathbf{r}) = \int |\chi_0(\mathbf{r}_e, \mathbf{r}_h)|^2 d\mathbf{r}_e$ and $\rho_h(\mathbf{r}) = \int |\chi_0(\mathbf{r}_e, \mathbf{r}_h)|^2 d\mathbf{r}_h$ are the electron and hole density, respectively. The calculated distribution map for $\rho(\mathbf{r})$ is shown in Fig. 3f. The laterally separated electrons and holes of the ICT excitons yield an alternating charge polarity that nicely matches our photocurrent map (Fig. 3c), providing quantitative spatial evidence that we are imaging ICT moiré excitons.

Discussion

We are able to explore the interaction between the STM tip and ICT moiré excitons by investigating the V_{bias} dependence of the photocurrent. Figure 4a shows the photocurrent as a function of V_{bias} measured at the AB (red, hole dominant) and B^{W/W} (blue, electron dominant) sites (with the same tip status as when measuring Fig. 3a,b). It shows a ~ 200 mV tip bias range (dashed lines) where positive photocurrent (at AB sites) and negative photocurrent (at B^{W/W} sites) coexist. To observe the tip's effect on the photocurrent, we measured photocurrent maps for $-985 \text{ mV} \leq V_{\text{bias}} \leq -602 \text{ mV}$ using the same tip status (Fig. 4b–f). These maps also show a ~ 200 mV range of V_{bias} values where positive and negative photocurrent coexist, consistent with Fig. 4a. This V_{bias} range varies depending on the tip sharpness but always lies between 100 mV and 250 mV (see the Supplementary Information for more V_{bias} dependent photocurrent maps).

The V_{bias} dependence of the photocurrent reflects a tip-induced exciton dissociation effect, as illustrated in Fig. 4g–i for different V_{bias} values. Because of capacitive coupling between the back gate graphite and the STM tip, a potential difference between them induces an electric field near the tip apex that perturbs the ICT moiré excitons (that is, a tip-induced band bending effect). The t-WS₂ chemical potential lies within an energy gap at $V_{\text{BG}} = 0$ and so does not screen the electric field. The work function difference between the tip (made of Pt/Ir) and the graphite back gate causes this field to be present even at $V_{\text{bias}} = 0$, but it can be cancelled by setting $V_{\text{bias}} = V_0$, where V_0 is the work function difference. At $V_{\text{bias}} - V_0 = 0$ (Fig. 4g), the tip exerts only a weak perturbation on the ICT excitons and the tip chemical potential is within the t-WS₂ bandgap. Therefore, a spatially alternating photocurrent polarity can be observed (Figs. 3c and 4c–e). However, at $V_{\text{bias}} - V_0 > 0$, the tip apex accumulates negative charge and attracts holes while repelling electrons (Fig. 4h). Above a certain threshold, this effect dissociates the ICT excitons and only a positive current can be observed as in Fig. 4f. Similarly, only a negative current is seen when $V_{\text{bias}} - V_0$ is much smaller than zero (Fig. 4b) owing to opposite dissociation of the ICT excitons, as illustrated in Fig. 4i.

In conclusion, our PTM enables real-space imaging of ICT moiré excitons with sub-nanometre spatial resolution. The observed electron and hole distributions agree well with *ab initio* *GW*-BSE calculation results. This work establishes a new approach for probing the microscopic behaviour of photoexcited states in 2D van der Waals heterostructures.

Online content

Any methods, additional references, Nature Portfolio reporting summaries, source data, extended data, supplementary information, acknowledgements, peer review information; details of author contributions and competing interests; and statements of data and code availability are available at <https://doi.org/10.1038/s41563-023-01753-4>.

References

- Li, H. et al. Imaging two-dimensional generalized Wigner crystals. *Nature* **597**, 650–654 (2021).
- Regan, E. C. et al. Mott and generalized Wigner crystal states in WSe₂/WS₂ moiré superlattices. *Nature* **579**, 359–363 (2020).
- Xu, Y. et al. Correlated insulating states at fractional fillings of moiré superlattices. *Nature* **587**, 214–218 (2020).
- Huang, X. et al. Correlated insulating states at fractional fillings of the WS₂/WSe₂ moiré lattice. *Nat. Phys.* **17**, 715–719 (2021).
- Xie, Y.-M., Zhang, C.-P., Hu, J.-X., Mak, K. F. & Law, K. T. Valley-polarized quantum anomalous Hall state in moiré MoTe₂/WSe₂ heterobilayers. *Phys. Rev. Lett.* **128**, 026402 (2022).
- Li, T. et al. Quantum anomalous Hall effect from intertwined moiré bands. *Nature* **600**, 641–646 (2021).
- Jin, C. et al. Observation of moiré excitons in WSe₂/WS₂ heterostructure superlattices. *Nature* **567**, 76–80 (2019).

8. Naik, M. H. et al. Intralayer charge-transfer moiré excitons in van der Waals superlattices. *Nature* **609**, 52–57 (2022).
9. Seyler, K. L. et al. Signatures of moiré-trapped valley excitons in MoSe₂/WSe₂ heterobilayers. *Nature* **567**, 66–70 (2019).
10. Tran, K. et al. Evidence for moiré excitons in van der Waals heterostructures. *Nature* **567**, 71–75 (2019).
11. Choi, Y. et al. Correlation-driven topological phases in magic-angle twisted bilayer graphene. *Nature* **589**, 536–541 (2021).
12. Kerelsky, A. et al. Maximized electron interactions at the magic angle in twisted bilayer graphene. *Nature* **572**, 95–100 (2019).
13. Jiang, Y. et al. Charge order and broken rotational symmetry in magic-angle twisted bilayer graphene. *Nature* **573**, 91–95 (2019).
14. Wong, D. et al. Cascade of electronic transitions in magic-angle twisted bilayer graphene. *Nature* **582**, 198–202 (2020).
15. Xie, Y. et al. Spectroscopic signatures of many-body correlations in magic-angle twisted bilayer graphene. *Nature* **572**, 101–105 (2019).
16. Cao, Y. et al. Correlated insulator behaviour at half-filling in magic-angle graphene superlattices. *Nature* **556**, 80–84 (2018).
17. Li, H. et al. Mapping charge excitations in generalized Wigner crystals. Preprint at *arXiv* <https://doi.org/10.48550/arXiv.2209.12830> (2022).
18. Kim, H. et al. Evidence for unconventional superconductivity in twisted trilayer graphene. *Nature* **606**, 494–500 (2022).
19. Oh, M. et al. Evidence for unconventional superconductivity in twisted bilayer graphene. *Nature* **600**, 240–245 (2021).
20. Cao, Y. et al. Unconventional superconductivity in magic-angle graphene superlattices. *Nature* **556**, 43–50 (2018).
21. Karni, O. et al. Structure of the moiré exciton captured by imaging its electron and hole. *Nature* **603**, 247–252 (2022).
22. Wang, L. et al. Correlated electronic phases in twisted bilayer transition metal dichalcogenides. *Nat. Mater.* **19**, 861–866 (2020).
23. Yankowitz, M. et al. Tuning superconductivity in twisted bilayer graphene. *Science* **363**, 1059–1064 (2019).
24. Li, H. et al. Imaging local discharge cascades for correlated electrons in WS₂/WSe₂ moiré superlattices. *Nat. Phys.* <https://doi.org/10.1038/s41567-021-01324-x> (2021).
25. Imai-Imada, M. et al. Orbital-resolved visualization of single-molecule photocurrent channels. *Nature* **603**, 829–834 (2022).
26. Wang, L., Xia, Y. & Ho, W. Atomic-scale quantum sensing based on the ultrafast coherence of an H₂ molecule in an STM cavity. *Science* **376**, 401–405 (2022).
27. Qiu, X., Nazin, G. & Ho, W. Vibrationally resolved fluorescence excited with submolecular precision. *Science* **299**, 542–546 (2003).
28. Čavar, E. et al. Fluorescence and phosphorescence from individual C₆₀ molecules excited by local electron tunneling. *Phys. Rev. Lett.* **95**, 196102 (2005).
29. Bolotov, L., Tada, T., Poborchiev, V., Fukuda, K. & Kanayama, T. Spatial distribution of photocurrent in Si stripes under tilted illumination measured by multimode scanning probe microscopy. *Jpn J. Appl. Phys.* **51**, 088005 (2012).
30. Yamamoto, H. Y. H., Kamiya, I. K. I. & Takahashi, T. T. Photoinduced current properties of InAs-covered GaAs studied by scanning tunneling microscopy. *Jpn J. Appl. Phys.* **38**, 3871 (1999).
31. Takeuchi, O. et al. Probing subpicosecond dynamics using pulsed laser combined scanning tunneling microscopy. *Appl. Phys. Lett.* **85**, 3268–3270 (2004).
32. McEllistrem, M., Haase, G., Chen, D. & Hamers, R. Electrostatic sample–tip interactions in the scanning tunneling microscope. *Phys. Rev. Lett.* **70**, 2471 (1993).
33. Kochanski, G. P. & Bell, R. STM measurements of photovoltage on Si(111) and Si(111):Ge. *Surf. Sci.* **273**, L435–L440 (1992).
34. Matthes, T. W. et al. Investigation of photoinduced tunneling current and local surface photovoltage by STM. *Appl. Surf. Sci.* **123**, 187–191 (1998).
35. Li, H. et al. Imaging moiré flat bands in three-dimensional reconstructed WSe₂/WS₂ superlattices. *Nat. Mater.* **20**, 945–950 (2021).
36. Naik, M. H. & Jain, M. Ultraflatbands and shear solitons in moiré patterns of twisted bilayer transition metal dichalcogenides. *Phys. Rev. Lett.* **121**, 266401 (2018).
37. Naik, M. H., Kundu, S., Maity, I. & Jain, M. Origin and evolution of ultraflat bands in twisted bilayer transition metal dichalcogenides: realization of triangular quantum dots. *Phys. Rev. B* **102**, 075413 (2020).
38. Wu, F., Lovorn, T. & MacDonald, A. H. Topological exciton bands in moiré heterojunctions. *Phys. Rev. Lett.* **118**, 147401 (2017).
39. Jin, C. et al. Ultrafast dynamics in van der Waals heterostructures. *Nat. Nanotechnol.* **13**, 994–1003 (2018).
40. Wang, H., Zhang, C. & Rana, F. Ultrafast dynamics of defect-assisted electron–hole recombination in monolayer MoS₂. *Nano Lett.* **15**, 339–345 (2015).
41. Shi, H. et al. Exciton dynamics in suspended monolayer and few-layer MoS₂ 2D crystals. *ACS Nano* **7**, 1072–1080 (2013).
42. Jauregui, L. A. et al. Electrical control of interlayer exciton dynamics in atomically thin heterostructures. *Science* **366**, 870–875 (2019).
43. Hybertsen, M. S. & Louie, S. G. Electron correlation in semiconductors and insulators: band gaps and quasiparticle energies. *Phys. Rev. B* **34**, 5390–5413 (1986).
44. Rohlfing, M. & Louie, S. G. Electron–hole excitations in semiconductors and insulators. *Phys. Rev. Lett.* **81**, 2312–2315 (1998).

Publisher's note Springer Nature remains neutral with regard to jurisdictional claims in published maps and institutional affiliations.

Springer Nature or its licensor (e.g. a society or other partner) holds exclusive rights to this article under a publishing agreement with the author(s) or other rightsholder(s); author self-archiving of the accepted manuscript version of this article is solely governed by the terms of such publishing agreement and applicable law.

© The Author(s), under exclusive licence to Springer Nature Limited 2024

Methods

Sample fabrication

The t-WS₂ device was fabricated using a micromechanical stacking technique⁴⁵. A poly(propylene) carbonate (PPC) film stamp was used to pick up all exfoliated 2D material flakes. The 2D material layers in the main heterostructure region were picked up in the following order: substrate hBN, graphite, bottom hBN, monolayer WS₂, twisted monolayer WS₂, graphene nanoribbon array. The graphene nanoribbon array serves as a contact electrode for the t-WS₂. The PPC film, together with the stacked sample, was peeled, flipped over and transferred onto a Si/SiO₂ substrate (SiO₂ thickness 285 nm). The PPC layer was subsequently removed using ultra-high-vacuum annealing at 330 °C, resulting in an atomically clean heterostructure suitable for STM measurements. A 50 nm Au and 5 nm Cr metal layer was evaporated through a shadow mask to form electrical contacts to graphene layers.

dI/dV spectroscopy measurements

A bias modulation having amplitude of 25 mV and frequency of 500–900 Hz was used to obtain the dI/dV signal. All the dI/dV spectra and maps in Fig. 2 were measured at $T = 5.4$ K. dI/dV mapping was performed under open-loop conditions with the tip height set by the following procedure: (a) we set tip the height at the condition $V_{\text{bias}} = 3.8$ V and $I = 10$ pA with closed feedback, then (b) we turned off the feedback and lowered the tip height by a distance of $h_{\text{tip}} = 50$ pm.

Auto laser alignment

To overcome laser misalignment induced by STM thermal drift during the PTM measurements (usually lasting ~10 h), a home-built auto laser alignment system with feedback control was developed. The laser spot position is detected with a camera and corrected via a piezo-driven mirror every 20 s.

PTM measurements

All the photocurrent tunnelling spectra and mapping shown in this work were measured at $T = 7.6$ – 7.7 K with a laser power ranging from 600 to 900 μ W. The photocurrent mapping was performed under open-loop conditions with the tip height set by the following procedures: (a) we set the tip height at a tip bias of V_{bias} and current setpoint of I , and (b) we turned off the feedback control and lowered the tip height by a distance of h_{tip} . The parameters for Fig. 3c were $V_{\text{bias}} = -3$ V, $I = 400$ pA and $h_{\text{tip}} = 0$. The parameters for Fig. 4b–f were $V_{\text{bias}} = -3$ V, $I = 200$ pA and $h_{\text{tip}} = 0$. The parameters used for the extended photocurrent map data are specified in the Supplementary Information.

Theoretical calculations

We studied a 57.72° twisted bilayer WS₂ moiré superlattice which contained 3,786 atoms in the unit cell. The structure was relaxed using classical force-field calculations. The relaxed configuration of atoms was used to study the electronic structure of the moiré superlattice. We constructed the BSE effective Hamiltonian using 12 valence and 50 conduction bands with $3 \times 3 \times 1$ k-point sampling of the moiré BZ. We used a greater number of conduction band states than valence band states owing to the larger density of states at the conduction band edge (Fig. 2a). The moiré kernel matrix elements of the BSE were computed using the generalized PUMP method as a coherent linear combination of pristine unit cell matrix elements (see Supplementary Information for details). We used a basis of 200 valence and 200 conduction states of each pristine layer to expand the moiré electronic wavefunctions. The static dielectric matrix used to compute the pristine unit cell kernel matrix elements was approximated to be identical to that of pristine 2H or AB stacking.

Data availability

The data supporting the findings of this study are included in the main text and in the Supplementary Information, and

are also available at <https://github.com/HongyuanLiCMP/Imaging-Moir-Excited-States-with-Photocurrent-Tunneling-Microscopy>.

References

45. Wang, L. et al. One-dimensional electrical contact to a two-dimensional material. *Science* **342**, 614–617 (2013).

Acknowledgements

This work was primarily funded by the United States Department of Energy, Office of Science, Office of Basic Energy Sciences, Materials Sciences and Engineering Division under contract no. DE-AC02-05CH11231 (van der Waals heterostructure programme KCFW16) for device fabrication, STM spectroscopy and force field calculations for structural reconstructions. The Center for Computational Study of Excited-State Phenomena in Energy Materials (C2SEPEM) at Lawrence Berkeley National Laboratory, supported by the United States Department of Energy, Office of Science, Basic Energy Sciences, Materials Sciences and Engineering Division under contract no. DE-AC02-05CH11231, as part of the Computational Materials Sciences Program, provided advanced codes and experimental support for optical measurements. The Theory of Materials Program (KC2301) funded by the DOE Office of Science, Basic Energy Sciences, Materials Sciences and Engineering Division under contract DE-AC02-05CH11231, provided resources to develop the PUMP approach and analysis of the moiré excitons. Computational resources were provided by the National Energy Research Scientific Computing Center (NERSC), which is supported by the DOE Office of Science under contract DE-AC02-05CH11231, and Frontera at TACC, which is supported by the National Science Foundation under grant OAC-1818253. Support was also provided by National Science Foundation Award DMR-2221750 (surface preparation). S.T. acknowledges support from DOE-SC0020653, NSF DMR 2111812, NSF DMR 1552220, NSF 2052527, DMR 1904716 and NSF CMMI 1933214 for WS₂ bulk crystal growth and analysis. K.W. and T.T. acknowledge support from JSPS KAKENHI (grant nos. 19H05790, 20H00354 and 21H05233). We thank Y. W. Choi, S. Kundu and J. Ruan for discussions.

Author contributions

S.G.L., M.F.C. and F.W. conceived the project. H.L. and Z.X. performed the STM/STS and PTM measurements, M.H.N. and F.H.d.J. formulated the generalized PUMP method, and M.H.N., W.K. and Z.L. performed the ab initio GW-BSE calculations. H.L. and Z.X. fabricated the heterostructure device. R.S., R.B. and S.T. grew the WS₂ crystals. K.W. and T.T. grew the hBN single crystal. All authors discussed the results and wrote the manuscript.

Competing interests

The authors declare no competing interests.

Additional information

Supplementary information The online version contains supplementary material available at <https://doi.org/10.1038/s41563-023-01753-4>.

Correspondence and requests for materials should be addressed to Steven G. Louie, Michael F. Crommie or Feng Wang.

Peer review information *Nature Materials* thanks the anonymous reviewers for their contribution to the peer review of this work.

Reprints and permissions information is available at www.nature.com/reprints.